# X-ray Crystal Structure of the Yeast Kar3 Motor Domain Complexed with Mg·ADP to 2.3 Å Resolution[†,‡]

Andrew M. Gulick,[§] Hebok Song,[||] Sharyn A. Endow,[||] and Ivan Rayment*[,§]

*Institute for Enzyme Research and Department of Biochemistry, University of Wisconsin, Madison, Wisconsin 53705, and Department of Microbiology, Duke University Medical Center, Durham, North Carolina 27710*

*Received October 9, 1997; Revised Manuscript Received December 1, 1997*

ABSTRACT: The kinesin family of motor proteins, which contain a conserved motor domain of ∼350 amino acids, generate movement against microtubules. Over 90 members of this family have been identified, including motors that move toward the minus or plus end of microtubules. The Kar3 protein from *Saccharomyces cerevisiae* is a minus end-directed kinesin family member that is involved in both nuclear fusion, or karyogamy, and mitosis. The Kar3 protein is 729 residues in length with the motor domain located in the C-terminal 347 residues. Recently, the three-dimensional structures of two kinesin family members have been reported. These structures include the motor domains of the plus end-directed kinesin heavy chain [Kull, F. J., et al. (1996) *Nature 380*, 550−555] and the minus end-directed Ncd [Sablin, E. P., et al. (1996) *Nature 380*, 555−559]. We now report the structure of the Kar3 protein complexed with Mg·ADP obtained from crystallographic data to 2.3 Å. The structure is similar to those of the earlier kinesin family members, but shows differences as well, most notably in the length of helix α4, a helix which is believed to be involved in conformational changes during the hydrolysis cycle.

Molecular motor proteins utilize the energy from ATP hydrolysis to generate force and move on actin filaments or microtubules (*1*). These fall into the superfamilies of myosins (*2*), dyneins (*3*), and kinesins (*3*, *4*). The known myosins are motors that move toward the fast polymerizing and depolymerizing end of actin filaments. The dyneins are minus end motors that move toward the more stable, slow-growing ends of microtubules. Most of the kinesins are plus end microtubule motors, but strikingly, some are minus end motors (*4*), like the dyneins. The plus- and minus end kinesins show sequence homology in the motor domain, a region of the protein that contains an ATP-binding consensus sequence (*5*) and a proposed microtubule-binding site (*6*). The motor domains of the plus- and minus end kinesins are highly conserved and show ∼40% sequence identity over an ∼350-residue region. Interestingly, the plus- and minus end kinesins differ in the location of the motor domain: The motor domain of the plus end kinesins is at the N terminus of the protein, whereas it is located at the C terminus of the minus end kinesins.

Recent work has suggested that the directionality of kinesin motors resides in the neck region that lies immediately after the motor domain of N-terminal motors and immediately before the motor domain of C-terminal kinesins. The motor domain of two plus end kinesins was replaced with the motor domain of the minus end kinesin Ncd (*7*, *8*). The resulting chimeric proteins retained the plus end directionality of the neck region, suggesting that a region outside the traditional motor domain is a determinant of directionality.

More than 90 kinesin proteins have been identified to date in nonmetazoan and metazoan organisms from the protist, fungal, plant, and animal kingdoms (*9*, *10*), leading to the expectation that these proteins will be found in all eukaryotes. The kinesin proteins perform diverse functions in organelle and vesicle transport, and chromosome and spindle motility in dividing cells (*4*). Genes for six kinesin proteins have been identified in *Saccharomyces cerevisiae* (*10*) and are likely to encode the full complement of kinesin proteins. One of these is the gene for the C-terminal motor kinesin, Kar3 (*11*).

The Kar3 kinesin protein is required for nuclear fusion, or karyogamy, during mating in yeast and also plays a role in mitosis. *kar3* mutants show a severe karyogamy defect, resulting in failure of nuclei in mating cells to fuse (*12*). Mitotically growing *kar3* mutant cells accumulate large budded cells with short spindles and a single nucleus, typical of mitotic arrest (*11*). Expression of Kar3 in bacteria as a fusion protein with glutathione *S*-transferase (GST[1]) followed by in vitro motility assays showed that Kar3 is a slow microtubule motor protein with a velocity of 1−2 μm/min and minus end polarity of movement on microtubules (*13*). The Kar3 motor also destabilizes taxol-stabilized microtubules in vitro, acting in a nucleotide-dependent manner and primarily at microtubule minus ends (*13*). The effect of Kar3

[†] This research was supported in part by NIH Grants AR35186 (I.R.) and GM46225 (S.A.E.) and American Cancer Society Grant CB-47 (S.A.E.). A.M.G. was supported by NRSA Fellowship AR08422.

[‡] The X-ray coordinates have been deposited in the Brookhaven Protein Data Bank (file name 3KAR).

* To whom correspondence should be addressed at Institute for Enzyme Research, 1710 University Ave., Madison, WI 53705. Phone: (608) 262-0529. Fax: (608) 265-2904. E-mail: ivan@enzyme.wisc.edu.

[§] University of Wisconsin.

[||] Duke University Medical Center.

[1] Abbreviations: GST, glutathione *S*-transferase; KHC, kinesin heavy chain.

S0006-2960(97)02504-X CCC: $15.00 
Published on Web 01/30/1998

on microtubule stability is likely to be important in vivo, where shortening of cross-bridged microtubules that lie between the haploid nuclei of mating cells has been proposed to help move the nuclei together for fusion (*13*). Kar3 may also regulate the length and number of spindle microtubules during mitotic growth (*11*, *14*, *15*).

The structures of the motor domains of two kinesin family members, plus end-directed human kinesin heavy chain (KHC) and minus end-directed Ncd, have recently been elucidated (*16*, *17*). These structures demonstrate that the core of the kinesin motor domain is an eight-stranded $\beta$-sheet flanked on both sides by three $\alpha$-helices. The protein contains a P-loop, a sequence seen frequently in nucleotide-binding proteins (*18*). The structure around the P-loop is similar to that seen in a number of nucleotide-binding proteins, including the G-proteins, $p21^{Ras}$ and transducin-$\alpha$, and the myosin proteins (*19*, *20*).

In this report, we present the three-dimensional structure of the Kar3 motor domain complexed with Mg·ADP solved to a resolution of 2.3 Å. There are several differences between the structures of the two minus end motors, Kar3 and Ncd, most notably in the small three-stranded $\beta$-sheet at the N terminus of the motor domain and in the orientation of several loops. Of the secondary structural elements, the largest difference is in helix $\alpha$4, which is much longer in the Kar3 structure than in either Ncd or KHC.

## METHODS

*Protein Purification.* The Kar3 motor domain protein was expressed in *Escherichia coli* from the plasmid pMW/Kar3 (*21*). pMW/Kar3 encodes residues 383−729 of Kar3, corresponding to the conserved motor domain (*4*). $Leu^{383}$ was changed to Met during plasmid construction. BL21-(DE3)pLysS host cells carrying pMW/Kar3 and pACYC184/*argU*$^+$ (*22*, *23*) were induced by addition of 0.4 mM IPTG followed by growth at 18 °C for 6 h. Protein was purified from cell pellets through the SP-Sepharose step, as described (*23*). The purified protein was active in ATPase assays and judged to be ∼95% pure by laser scanning densitometry of a Coomassie Blue-stained SDS−polyacrylamide gel. The mass of the protein as determined by electrospray ionization mass spectroscopy was 38 915.6 ± 6.9 Da, in close agreement with the mass of 38 912.46 Da predicted from the amino acid sequence.

Proteins from several SP-Sepharose chromatographic experiments were pooled. ATP was added to the protein solution to a concentration of 1 mM to increase solubility, and the protein was dialyzed against 150 mM NaCl, 1 mM $MgCl_2$, 0.2 mM $NaN_3$, 1 mM DTT, and 10 mM Hepes at pH 7.5 and 4 °C. The protein was concentrated to ∼11 mg/mL and rapidly frozen as pellets by dropping 30−50 $\mu$L aliquots into liquid nitrogen. Freshly thawed aliquots were used for crystallization experiments.

*Crystallization.* Crystals were grown by microbatch experiments at room temperature. Mg·ADP was added to the protein to a final concentration of 2 mM. Equal volumes of protein and precipitant were combined and were streak-seeded immediately from crushed crystals with a cat whisker. The precipitant solution consisted of 22% methyl ether PEG 2000, 100 mM NaCl, 2% ethylene glycol, and 50 mM Hepes at pH 7.0. Crystals grew as thin pyramids with a base of 0.1 × 1.0 mm and a height of 0.5 mm to a maximum size within 2−3 weeks. Kar3 crystallized in the monoclinic space group $P2_1$ with the following unit cell dimensions: $a = 44.1$ Å, $b = 81.2$ Å, $c = 48.3$ Å, and $\beta = 105.8°$. There is one Kar3 molecule in the asymmetric unit giving a Matthews coefficient of 2.14 (42% solvent) (*24*). The crystals were transferred to a stabilization solution containing 17% methyl ether PEG 2000, 150 mM NaCl, 1.5 mM $MgCl_2$, 1.0 mM ADP, 2% ethylene glycol, and 50 mM Hepes at pH 7.0. For heavy atom derivative data collection, the crystals were transferred directly into the stabilization solution containing compounds at the concentrations described in Table 1. Crystals were mounted in quartz capillary tubes and chilled to −4 °C for data collection.

Table 1: X-ray Diffraction Data

| | native | TELA | $K_2IrCl_6$ | MeHgCl |
|---|---|---|---|---|
| resolution (Å) | 2.3 | 2.4 | 2.4 | 2.7 |
| *R*merge[a] (%) | 3.4 | 7.4 | 5.8 | 5.6 |
| highest shell[b] (%) | 7.4 | 13.7 | 17.5 | 13.5 |
| no. of reflections | 43 898 | 63 211 | 57 073 | 27 306 |
| no. of independent reflections | 22 220 | 17 212 | 19 517 | 14 591 |
| completeness (%) | 93.2 | 95.0 | 92.3 | 93.1 |
| highest shell[b] (%) | 84.7 | 87.2 | 82.9 | 85.1 |
| unit cell dimensions | | | | |
| *a* (Å) | 44.1 | 44.1 | 44.2 | 44.1 |
| *b* (Å) | 81.2 | 81.5 | 80.7 | 81.7 |
| *c* (Å) | 48.3 | 48.4 | 48.3 | 48.5 |
| $\beta$ (deg) | 105.8 | 105.7 | 105.8 | 105.5 |
| heavy atom concentration (mM) | | 2.0 | 2.5 | 0.5 |
| length of soak | | 46 h | 16 h | 30 min |
| $R_{iso}$[c] (%) | | 16.6 | 14.7 | 21.9 |
| phasing power[d] | | 1.06 | 1.18 | 1.00 |
| no. of sites | | 4 | 3 | 2 |

[a] $R_{merge} = \sum(||I_{hi}|-|I_h||)/\sum I_{hi} \times 100$, where $I_{hi}$ and $I_h$ are the intensities of individual and mean structure factors, respectively. [b] The highest-resolution shell for native is 2.4−2.3 Å, triethyllead acetate is 2.5−2.4 Å, $K_2IrCl_6$ is 2.5−2.4 Å, and methyl mercuric chloride is 2.8−2.7 Å. [c] $R_{iso} = \sum(||F_h|-|F_n||)/\sum|F_n| \times 100$, where $F_h$ and $F_n$ are the heavy atom and native structure factors, respectively. [d] The phasing power is defined as the mean value of the heavy atom structure factor divided by the lack-of-closure error. The anomalous signals were collected for the TELA and $K_2IrCl_6$ data sets and were used in refinement of heavy atom positions. The overall figure of merit for the data to 2.6 Å was 0.55.

*Data Collection and Structure Refinement*. Data were collected with a Siemens Hi-star area detector with CuK$\alpha$ radiation from a Rigaku RU200 X-ray generator operating at 50 kV and 90 mA with Supper long double-focusing mirrors. Cooled wet crystals diffracted well to 2.3 Å resolution (Table 1). Data were processed with XDS (*25*, *26*), merged, and scaled internally with XSCALIBRE (*27*).

Initially, attempts were made to solve the structure by molecular replacement with the program AMORE (*28*, *29*) starting from either the KHC or Ncd motor domain as a search model (*16*, *17*). Search models included the entire motor domain molecule and models from which nonconserved side chains and presumed loops were removed. Although unique solutions were determined, attempts to build and refine a model based on these maps proved unsuccessful. Even when the model was pared back to a core consisting of the central sheet and a few well ordered helices, the maps proved to be of insufficient quality to determine and refine the structure.

To obtain independent phase information, a search was made for isomorphous heavy atom derivatives. Three heavy

Table 2: Refinement Data

| | |
|---|---|
| total no. of atoms | 2609 |
| no. of protein atoms | 2476 |
| no. of solvent atoms | 105 |
| average *B*-factor[a] | 38.7 Å$^2$ |
| average *B*, protein | 38.8 Å$^2$ |
| average *B*, main chain | 34.8 Å$^2$ |
| average *B*, solvent | 40.4 Å$^2$ |
| average *B*, nucleotide | 25.9 Å$^2$ |
| *R*-factor[b] | 17.5% |
| rms deviation | |
| bond lengths | 0.016 Å |
| bond angles | 2.15° |
| trigonal planes | 0.006 Å |
| general planes | 0.015 Å |
| contacts | 0.096 Å |

[a] Average *B*-factors are reported for all non-hydrogen atoms. [b] *R*-factor $= \sum(||F_{obs}|-|F_{calcd}||)/\sum|F_{obs}| \times 100$.

atom derivatives were identified (Table 1). A single major heavy atom binding site was identified readily by Fourier techniques for the triethyllead acetate derivative from a difference map calculated with phases from the molecular replacement solution core sequence. From this major site, an additional minor site was found by difference Patterson function refinement (*30*). The locations of the heavy atom binding sites in the remaining two derivatives were identified from difference Fourier maps starting with the phases calculated from the lead derivative. The three derivatives were refined with HEAVY, and MIR phases were generated (*30*). Two maps were examined, a native MIR map that was independent of the molecular replacement model and a SIGMAA (*31*) map in which the phases calculated from the molecular replacement core were combined with the MIR phases. The native MIR map was determined to be of better quality and was used for manually building the model with the program FRODO (*32*) on an Evans and Sutherland PS390 instrument.

Protein phases were calculated once 139 residues had been built into the MIR electron density map. This phase information was then combined with the heavy atom phases with SIGMAA weighting to give an improved electron density map (*31*). The model was subjected to its first round of least-squares refinement (*33*) once 208 residues had been built. After 15 cycles, the crystallographic *R*-factor dropped from 45.7 to 33.3% for the data to 2.6 Å. This value was better than the value that had been obtained during refinement

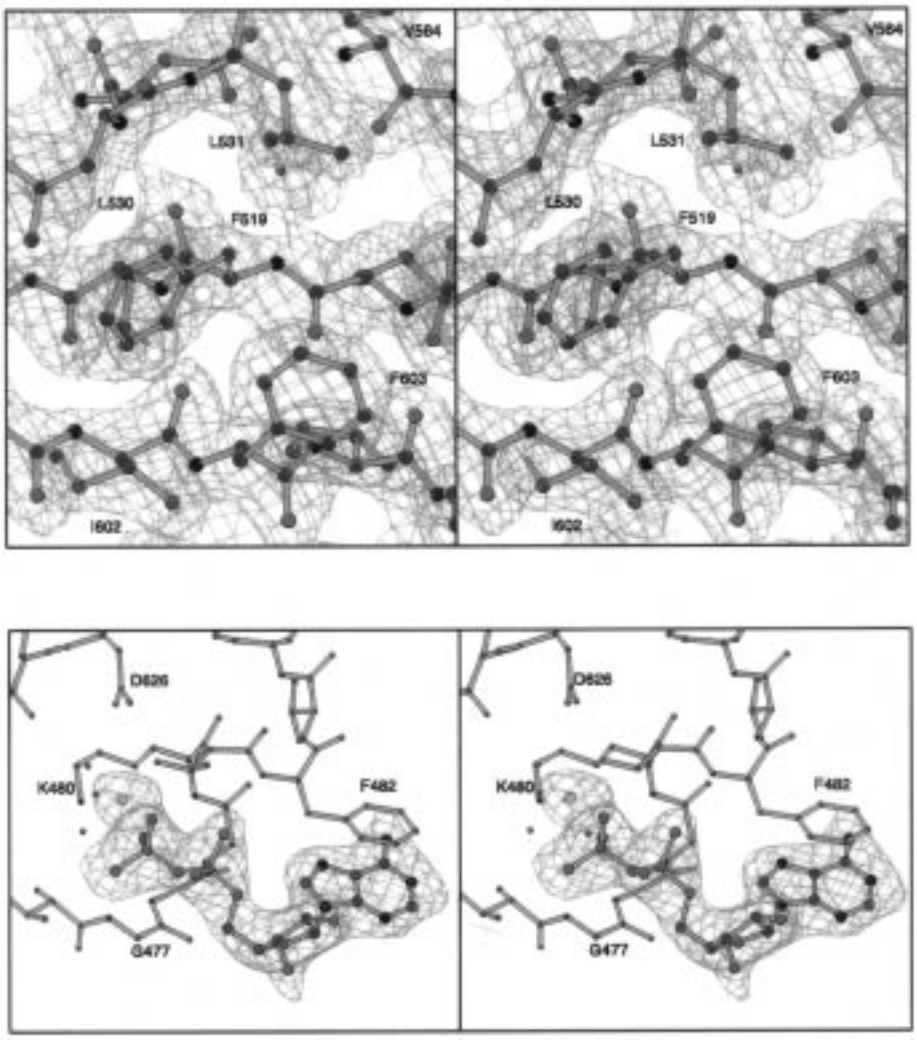


FIGURE 1: Stereodiagram of (A, top) the representative protein electron density and (B, bottom) the difference density for the Mg·ADP. Panel A shows a portion of the central $\beta$-sheet ($\beta$4 and $\beta$6) together with a portion of $\beta$5 and the loop that interrupts this strand. The map was calculated with coefficients of the form $2F_o - F_c$ contoured at 1.0$\sigma$. Panel B shows the electron density for the nucleotide when omitted from one cycle of refinement. The map was calculated with coefficients of the form $F_o - F_c$ and is contoured at 3.0$\sigma$. Figures 1−4 were generated with the program MOLSCRIPT (*41*).

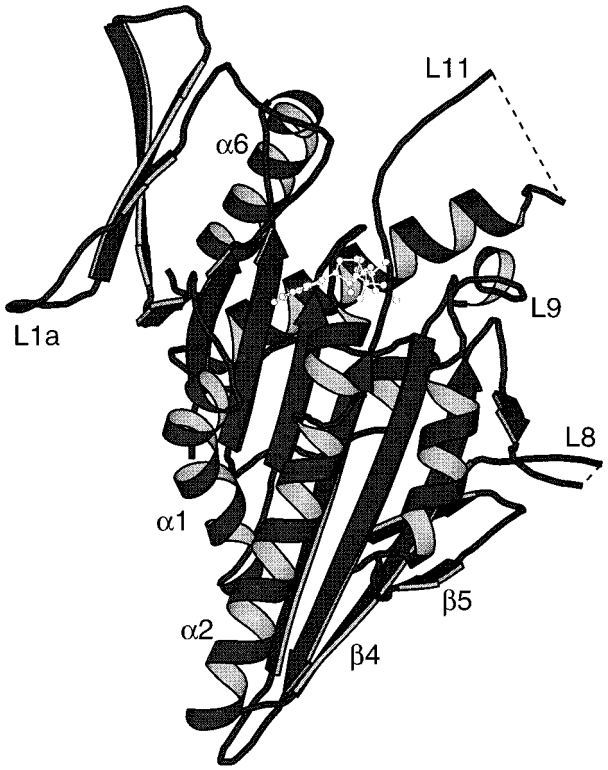


FIGURE 2: Ribbon diagram of the Kar3 protein motor domain showing the core eight-stranded $\beta$-sheet structure with flanking α-helices. The nucleotide binding pocket is shown at the top of the figure containing a molecule of Mg·ADP (white atoms). The two breaks in the protein model are illustrated with dashed lines.

attempts with the original molecular replacement solution. Least-squares refinement and phase combination were repeated as the model was completed. During this time, the resolution was extended to 2.3 Å. Water molecules were built into the model at locations where electron density was higher than 2.5$\sigma$ in the $F_o - F_c$ map and where appropriate stereochemistry was observed. Continued refinement and model building against maps calculated with protein phases reduced the *R*-factor to 17.5% against data to 2.3 Å. The final model contains 323 amino acid residues and 105 water molecules (Table 2). In the final model, 89 and 11% of the residues lie in the most favored and allowed portion of the Ramachandran plot as judged by PROCHECK (*34*) and TNT (*33*).

## RESULTS AND DISCUSSION

*Kar3 Structure*. The Kar3 structure was solved by a combination of molecular replacement and phases from three heavy atom derivatives. The C-terminal half of the Kar3 protein, residues Leu$^{383}$−Lys$^{729}$, contains the motor domain of the protein and was used for crystallization. The final model contains residues Gly$^{385}$−Ser$^{533}$, Leu$^{545}$−Ser$^{636}$, and Asp$^{641}$−Ser$^{722}$. There are two disordered loops that were not built into the model. The final model also contains a molecule of Mg·ADP and 105 water molecules. The average temperature factor for protein atoms is 38.8 Å$^2$, for protein main chain atoms is 34.8 Å$^2$, while for solvent molecules is 40.4 Å$^2$ (Table 2). Representative electron density is shown in Figure 1.

Several regions of the protein are poorly ordered in the structure. The side chains of residues Lys$^{398}$, Leu$^{400}$, Asp$^{404}$, Glu$^{412}$, Asn$^{416}$, Lys$^{579}$, Lys$^{580}$, Leu$^{584}$, Thr$^{587}$, Lys$^{613}$, Arg$^{644}$, Lys$^{651}$, Thr$^{669}$, Lys$^{670}$, Arg$^{671}$, Lys$^{719}$, Val$^{720}$, Asn$^{721}$, and Ser$^{722}$ are disordered and have been built as alanine residues in the current model. All of these residues lie on the surface of the protein; many are on loops. Residues Asp$^{667}$−His$^{672}$ are poorly ordered in the crystal lattice; as such, an occupancy of 0.5 was applied to this region of the protein during refinement. Electron density for loops L1 and L1a is weak but of sufficient quality to be built into the current model.

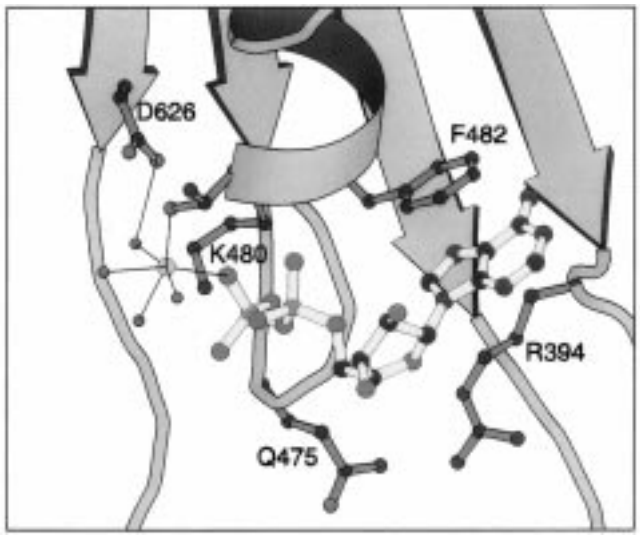


FIGURE 3: Ribbon diagram illustrating the active site, or P-loop, of the Kar3 molecule and the interactions of protein with the Mg·ADP molecule. The orientation has been rotated ~180° in the plane of the figure relative to the view shown in Figure 2. This results in the strands ($\beta$7, $\beta$3, $\beta$8, and $\beta$1 from left to right) pointing down toward the bottom of the figure rather than up, as seen in Figure 2. This view of the nucleotide binding pocket is commonly used for the G-proteins as well as the myosins. The side chains of Arg$^{394}$, Gln$^{475}$, Lys$^{480}$, Thr$^{481}$, Phe$^{482}$, and Asp$^{626}$ are also included. The $Mg^{2+}$ ion is shown in orange.

The predominant structural feature of the Kar3 motor domain is a central, mostly parallel, eight-stranded $\beta$-sheet (Figure 2). The strands have been numbered consecutively from the N terminus of the protein, in keeping with the system described by Fletterick and co-workers for KHC and Ncd (*16*, *17*). Within the sheet, the order of the strands is $\beta$2, $\beta$1, $\beta$8, $\beta$3, $\beta$7, $\beta$6, $\beta$4, and $\beta$5, with strands 5 and 6 oriented antiparallel to the remaining strands. Near strand $\beta$2 is a three-stranded antiparallel sheet containing strands $\beta$1a, $\beta$1b, and $\beta$1c. The plane of this sheet is nearly perpendicular to the plane of the central sheet. Strand $\beta$5 is interrupted by loop L8 which contains a disordered region at residues Asp$^{534}$−Gly$^{544}$ followed by the two antiparallel strands, $\beta$5a and $\beta$5b.

Three α-helices, also numbered from the N to C terminus, are located on each side of the $\beta$-sheet. Helices α1, α2, and α3 are located on the same side of the sheet as the active site, while the final three helices are on the opposite face. The first helix, α1, contains a bend at Val$^{455}$, where $\varphi = -96°$ and $\psi = -28°$. Interestingly, Ncd accomplishes this bend with a Pro residue at position 417 (*16*). There is an interruption at the second turn of α2, where an insertion of the sequence Asn$^{486}$-Pro-Gly-Asp-Gly-Ile-Ile introduces a $\beta$-turn into the helix. The helix resumes with residue Pro$^{493}$ and continues for 18 residues. Including the insertion, the entire α2 helix is 30 residues long, and stretches 37 Å,

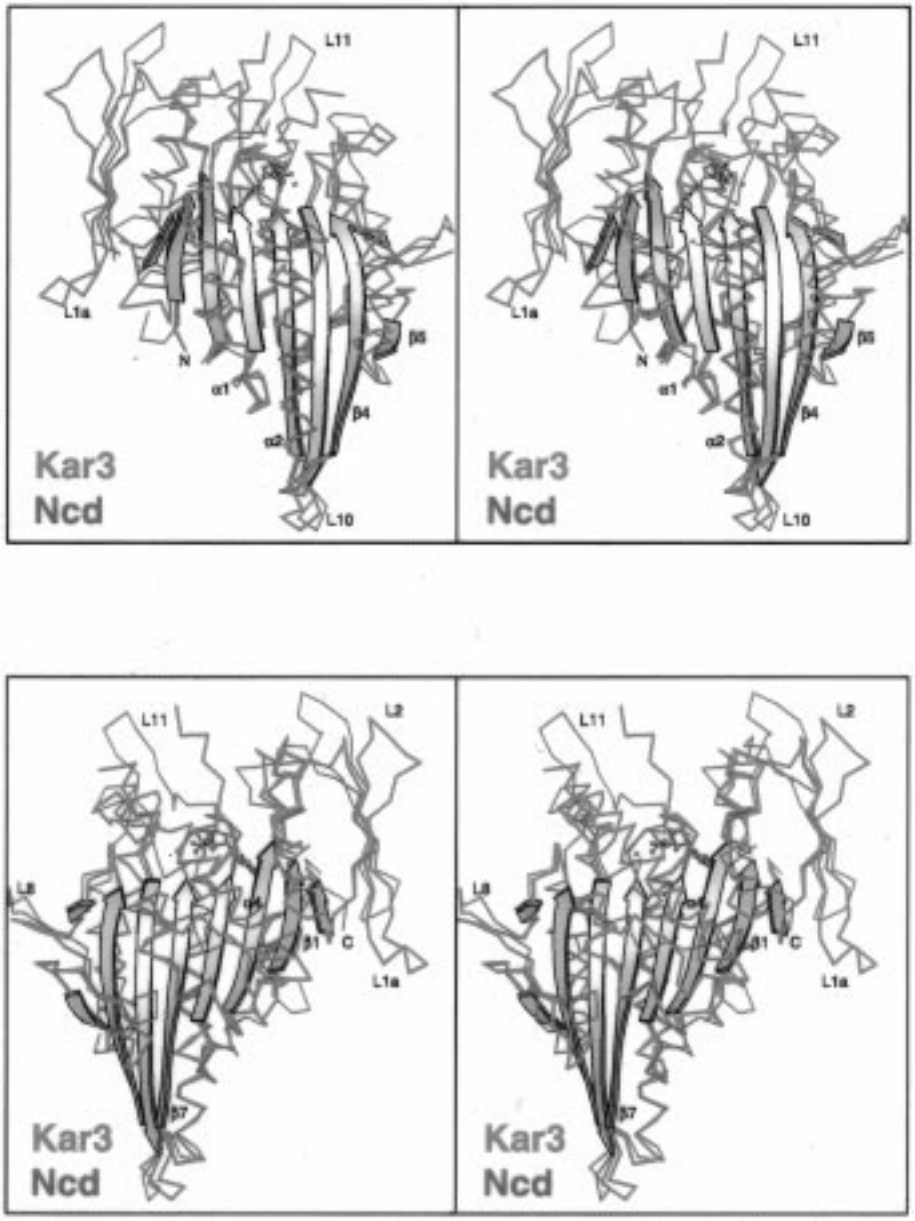


FIGURE 4: Stereodiagram overlap of Kar3 and Ncd motor domains from two perspectives. Because the central $\beta$-sheet of the two proteins is so similar, only the strands from Kar3 are depicted. The Kar3 protein C$\alpha$ tracing is shown in red, thicker lines; the Ncd protein is shown in blue. The upper figure shows the "front" of the protein, the side of the main sheet on which the nucleotide binding site is located. The lower figure is a view from the "back" side of the central $\beta$-sheets.

reaching from the P-loop (see below) to the end of the longest strands of the central sheet.

*Active Site of the Kar3 Motor Domain*. The active site of the Kar3 motor domain (Figure 1B) contains Mg·ADP where the P-loop wraps around the phosphates of the substrate (Figure 3). The P-loop, loop L4, follows the $\beta$3 strand of the central sheet and precedes the $\alpha$2 helix. The $Mg^{2+}$ ion is complexed by six oxygen atoms: a substrate oxygen on the $\beta$-phosphate, the side chain oxygen of $Thr^{481}$, and four water molecules. The 2′ and 3′ hydroxyls of the nucleotide point toward the solvent. A pocket for the adenine ring is formed by the side chain of $Phe^{482}$, the side chains of $Arg^{394}$ and $Pro^{395}$, and the side chains and main chain atoms of $Asp^{446}$−$Asn^{448}$. The adenine ring is stacked against the side chain of $Phe^{482}$. There are no direct hydrogen bonding interactions from protein to the adenine and ribose portions of the nucleotide. By contrast, there are numerous interactions with the phosphate portion of the nucleotide. An oxygen on the $\alpha$-phosphate forms a hydrogen bond to the amide nitrogen of $Phe^{482}$. One $\beta$-phosphate oxygen interacts with the amide nitrogen of $Gly^{477}$. The remaining oxygen on the $\beta$-phosphate that does not coordinate the $Mg^{2+}$ ion interacts with both the amide nitrogen and the side chain amino group of $Lys^{480}$. There are also several well-ordered water molecules present in the region of the phosphate groups.

*Comparison of the Kar3 Motor Domain to Ncd.* The Kar3 protein is structurally very similar to the Ncd protein (Figure 4). The amino acid sequences of the motor domains of the two proteins are 46% identical. Alignment of the 204 homologous $\alpha$-carbons showed that the proteins have an rms deviation of 1.0 Å. This alignment demonstrates that the main secondary structural elements are well conserved between the two proteins. The eight strands of the central

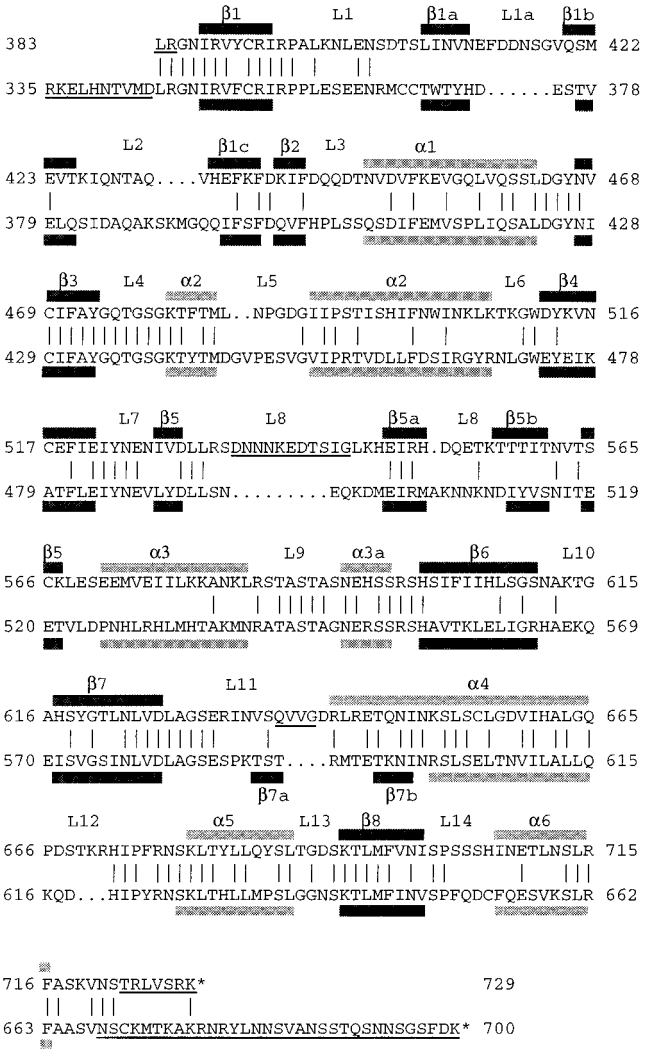


FIGURE 5: Amino acid alignment of Kar3 and Ncd motor domains. A structure-based alignment is shown which demonstrates the major differences in the lengths of secondary structure elements and adjoining loops. The α-helices are shown in gray, while the $\beta$-sheets are shown in black. The residues which are disordered in the two structures are underlined.

$\beta$-sheet superimpose very well. Of the main secondary structural elements, the only features that differ are helices α3 and α4. The α4 helix is much longer in Kar3 than in Ncd (Figure 5) or KHC. The region preceding this helix in Kar3 is disordered, whereas in Ncd, there is an antiparallel loop, loop L11, composed of strands $\beta$7a and $\beta$7b. This section of Ncd, loop L11 and helix α4, has been proposed to undergo movement during ATP hydrolysis, on the basis of the similarity in their positions to the "switch II" region of G-proteins and the poor packing of helix α4 (*16*). Although a portion of the Kar3 protein is disordered in this region, it is clear that there will not be a loop similar to that seen in Ncd since the extended N terminus of the α4 helix in Kar3 corresponds to the residues that form loop $\beta$7b in Ncd. Human KHC contains a short α4 helix, similar to that of Ncd. This may be relevant to the slower velocity of Kar3, compared to those of Ncd and KHC.

The small three-stranded $\beta$-sheet, $\beta$1, near the N terminus of the motor domain also differs between Kar3 and Ncd. While the strands are in similar positions, the loops between the strands are different lengths in the two proteins, changing the relative orientation of this domain. The loop L1a joining $\beta$1a to $\beta$1b is much longer in Kar3 than in Ncd. By contrast, loop L2 joining $\beta$1b to $\beta$1c is longer in Ncd than in Kar3 (Figures 4 and 5). This has the effect of rotating this domain in Kar3 so that it is farther away from the α6 helix. In Ncd, this domain nearly forms a lid that folds over helix α6.

Another difference between the Kar3 motor domain and the motor domains of both Ncd and KHC is the length of loop L5 that interrupts helix α2. In Kar3, this loop is six residues long, $Leu^{485}-Gly^{490}$. In Ncd, the loop is two residues longer, encompassing $Asp^{445}-Gly^{452}$. This interruption of the helix appears to be functionally important, as suggested by the *ncd*[2] mutation in this region of Ncd which changes $Gly^{446}$ to Arg and causes a complete loss of protein function (*35*). There is no homologous residue in Kar3, which is missing the conserved glycine at the base of loop L5 toward the N terminus (Figure 5). In human KHC, the L5 loop is even longer, $Glu^{96}-Gly^{106}$. In the three current models for kinesin protein motor domains, in which the protein is in the ADP conformation, the axis of the α2 helix is nearly straight; if the six-residue loop L5 in Kar3 were replaced by two alanine residues, this region of the protein would form a quite natural helix. It is tempting to speculate that this region of the protein must undergo a conformational change associated with the hydrolysis cycle. Loop L5 forms part of the entrance to the nucleotide-binding cleft. The openness of the entry to the cleft could help regulate binding of ATP and release of ADP and $P_i$ following hydrolysis.

It has been noted that the main structural features of KHC are very similar to secondary structure elements of myosin (*17*). Interestingly, the myosin proteins contain an interrupted helix motif similar to that noted above for helix α2 in the kinesin proteins, however not at the homologous helix. In myosin proteins, the interrupted helix is on the lower domain of the 50 kDa region of the protein rather than the helix which follows the P-loop of the protein. In the *Dictyostelium* myosin motor domain, S1dC, this helix runs from residue $Asp^{505}$ to $Val^{534}$ with the interruption occurring at residues $Gly^{519}-Gly^{524}$ (*36*). The myosin interruption loop contains an interesting Pro-Pro sequence in which the first Pro residue is in the cis conformation, $Gly^{519}$-Arg-Gln-cPro-Pro-$Gly^{524}$.

The orientation of the α3 helix is different among the three kinesin family members. Similarly, loop L9, which connects α3 to α3a, is altered among the three structures. In the three proteins, the lengths of loop L9 are the same but the orientations of these residues are quite different. In Kar3, loop L9 turns toward the active site, allowing the side chain of $Asn^{593}$, and possibly the carbonyl oxygen of $Arg^{585}$, to participate in the hydrogen bonding network near the phosphates of the substrate. By contrast, the L9 loops of Ncd and KHC are positioned farther away from the active site such that the protein atoms are over 7 Å away from the substrate. This results partly from the orientation of helix α3 and partly from the path that the L9 loops take after terminating the helix. The α3a helix ends at $Ser^{596}$-Ser-Arg, the sequence analogous to the switch I element in the G-proteins (*20*). On this basis, it is likely that this region is important for observed differences in the nucleotide hydrolysis rates of the three proteins.

*Mutations Identified in the Kar3 Protein.* A number of mutations in the *kar3* gene have been identified genetically

Table 3: *kar3* Mutants

| mutant | amino acid change | structural element affected | phenotype |
|---|---|---|---|
| *kar3*-894 | N378K | neck region | missense suppressor of *cin8ts kip1*Δ (*38*) |
| *kar3*-891 | S462L | α1 | missense suppressor of *cin8ts kip1*Δ (*38*) |
| *kar3*-1 | G479E | L4 (P-loop) | semidominant *kar3* karyogamy mutant (*12*) |
| *kar3*-893 | E521D | β4 | missense suppressor of *cin8ts kip1*Δ (*38*) |
| *kar3*-899 | R550S | β5a | missense suppressor of *cin8ts kip1*Δ (*38*) |
| *kar3*-8912 | T558A | β5b | missense suppressor of *cin8ts kip1*Δ (*38*) |
| *kar3*-898 | N650K | α4 | dominant missense suppressor of *cin8ts kip1*Δ, recessive karyogamy and meiotic mutant (*38*) |
| *kar3*-897 | V659L | α4 | missense suppressor of *cin8ts kip11*Δ (*38*) |

(Table 3). The original *kar3-1* mutant was shown to contain a single point mutation, G479E, in the P-loop region of the protein (*11*). This results in a semidominant karyogamy phenotype. Substitution of glutamic acid for glycine adjacent to the catalytic lysine in the nucleotide-binding cleft of the motor is likely to cause the motor to fail to bind to ATP. $Gly^{479}$ adopts a conformation ($\varphi = 105°$ and $\psi = 37°$) that is unfavorable for other amino acids, suggesting that the Gly to Glu mutation perturbs the secondary structure in this region. The mutant protein is thought to interfere with wild-type protein by binding to microtubules in rigor (*11*).

During mitosis in yeast, two counteracting forces have been proposed to act on the spindle pole bodies (*15*, *37*). The Cin8/Kip1 kinesin proteins are thought to produce an outward force on the spindle poles that is opposed by Kar3. Elimination of Cin8 and Kip1 activity results in the rapid collapse of the mitotic spindle with the previously separated poles being drawn together (*37*). The effects of the *cin8/kip1* mutations can be suppressed by a deletion of *kar3*. Additionally, a number of point mutations in *kar3* have been identified that suppress the *cin8/kip1* mutations (Table 3). These mutations all map to the Kar3 motor domain, but do not simply represent inactivation of Kar3 function as the cells, with the exception of *kar3-898*, do not exhibit defects in karyogamy and meiosis. This suggests that either the mutations have mild effects on Kar3, so that they do not dramatically alter the ability of Kar3 to function in essential cell processes, or the mutations cause a gain of function that allows the Kar3 to complement the missing Cin8/Kip1 activity (*38*). This second possibility is supported by the dominant nature of several of the mutations (Table 3). In either case, the regions of the protein identified by these mutations, namely the neck region, α1, β4, β5a, β5b, and α4, are undoubtedly important for function of Kar3 and other kinesin motor proteins. The neck region may determine or bias the directionality of motor movement (*7*, *8*).

*Microtubule Interactions of the Kinesin Motor Proteins.* Very recently, the regions of the kinesin motor proteins that interact with microtubules have been identified. The important protein residues were determined by alanine-scanning mutagenesis on human KHC (*39*) and by manual fitting of the Ncd model into electron density maps determined by cryoelectron microscopy of Ncd-decorated microtubules (*40*). The two methods independently gave very similar results. The microtubule binding site lies on a patch of electropositive residues located on several loops on the side of the β-sheet composed primarily of the C-terminal helices. The interaction residues come from four secondary structural elements: (a) the L7/L8 loops, (b) loop L11 and the N terminus of helix α4, (c) loop L12 and the start of helix α5, and (d) the α6 helix and the L2 loop. The final interaction was only noted in the cryo-EM reconstruction and was suggested to be relevant to the minus end specificity of Ncd (*40*). The availability of a second structure of a minus end specific protein now allows further analysis of these results.

As noted above, the overall secondary structure of Kar3 is very similar to both Ncd and KHC. Many positively charged residues are conserved, and the electropositive nature of the interface is intact in the Kar3 protein. The L12 loop of Kar3 is three residues longer than both Ncd (Figure 5) and KHC. This insertion, however, occurs at the start of loop L12 so that the residues which are involved in microtubule binding for KHC, $Tyr^{274}-Arg^{284}$, are conserved in location like the residues from Kar3, $His^{672}-Tyr^{682}$. Although portions of loop L11 are disordered, from the modeled portions, we can see that L11 of Kar3 is more similar to KHC than to Ncd. This suggests that this region of the microtubule binding domain is not specific to the minus or plus end specificity of the motor.

The L11 loop of KHC has been hypothesized to bind in the groove between protofilaments of the microtubule (*40*). The difference between Kar3 and Ncd in this region may be relevant to the ability of Kar3 to destabilize microtubules (*13*). The shorter length of L11 in Kar3 may result in the motor core binding deeper into the groove between protofilaments. This could cause the protofilaments at the microtubule ends to separate when the motor is bound to the microtubule, leading to the loss of curled fragments from protofilament ends.

The L2 loop of Ncd was suggested to be involved in minus end specific contacts because this loop is 10 residues longer in Ncd than in KHC (*40*). In Kar3, this loop is intermediate in size between the loops of KHC and Ncd (Figures 4 and 5). Together with the changes in helix α4 described above, this may play a role in the slower gliding velocity of Kar3 when compared to that of either KHC or Ncd.

## ACKNOWLEDGMENT

The authors gratefully acknowledge R. J. Fletterick and R. D. Vale for the coordinates for human KHC and Ncd motor domains, and helpful and stimulating discussions.

## REFERENCES

1. Goodson, H. V., Valetti, C., and Kreis, T. E. (1997) *Curr. Opin. Cell Biol. 9*, 18−28.
2. Sellers, J. R., Goodson, H. V., and Wang, F. (1996) *J. Muscle Res. Cell Motil. 17*, 7−22.
3. Hackney, D. D. (1996) *Annu. Rev. Physiol. 58*, 731−750.
4. Bloom, G. S., and Endow, S. A. (1994) in *Protein Profile*, Vol. 1, pp 1059−1116, Academic Press, London.
5. Walker, J. E., Saraste, M., Runswick, M. J., and Gay, N. J. (1982) *EMBO J. 1*, 945−951.
6. Yang, J. T., Laymon, R. A., and Goldstein, L. S. B. (1989) *Cell 56*, 879−889.

7. Case, R. B., Pierce, D. W., Hom-Booher, M., Hart, C. L., and Vale, R. D. (1997) *Cell 90*, 959−966.
8. Henningsen, U., and Schliwa, M. (1997) *Nature 389*, 93−96.
9. Goodson, H. V., Kang, S. J., and Endow, S. A. (1994) *J. Cell Sci. 107*, 1875−1884.
10. Greene, E. A., Henikoff, S., and Endow, S. A. (1997) http://www.blocks.fhcrc.org/∼kinesin/.
11. Meluh, P. B., and Rose, M. D. (1990) *Cell 60*, 1029−1041.
12. Polaina, J., and Conde, J. (1982) *Mol. Gen. Genet. 186*, 253−258.
13. Endow, S. A., Kang, S. J., Satterwhite, L. L., Rose, M. D., Skeen, V. P., and Salmon, E. D. (1994) *EMBO J. 13*, 2708−2713.
14. Roof, D. M., Meluh, P. B., and Rose, M. D. (1991) *Cold Spring Harbor Symp. Quant. Biol. 55*, 693−703.
15. Saunders, W., Hornack, D., Lengyel, V., and Deng, C. (1997) *J. Cell Biol. 137*, 417−431.
16. Sablin, E. P., Kull, J. F., Cooke, R., Vale, R. D., and Fletterick, R. J. (1996) *Nature 380*, 555−559.
17. Kull, F. J., Sablin, E. P., Lau, R., Fletterick, R. J., and Vale, R. D. (1996) *Nature 380*, 550−555.
18. Saraste, M., Sibbald, P. R., and Wittinghofer, A. (1990) *Trends Biochem. Sci. 15*, 430−434.
19. Smith, C. A., and Rayment, I. (1996) *Biophys. J. 70*, 1590−1602.
20. Vale, R. D. (1996) *J. Cell Biol. 135*, 291−302.
21. Song, H., and Endow, S. A. (1996) *Biochemistry 35*, 11203−11209.
22. Spanjaard, R. A., Chen, K., Walker, J. R., and van Duin, J. (1990) *Nucleic Acids Res. 18*, 5031−5036.
23. Song, H., and Endow, S. A. (1997) *BioTechniques 22*, 82−85.
24. Matthews, B. W. (1968) *J. Mol. Biol. 33*, 491−497.
25. Kabsch, W. (1988) *J. Appl. Crystallogr. 21*, 916−924.
26. Kabsch, W. (1988) *J. Appl. Crystallogr. 21*, 67−71.
27. Wesenberg, G., and Rayment, I. (1997) *XSCALIBRE: A System for Scaling and Merging X-ray Data*, University of Wisconsin, Madison, WI.
28. Rossman, M. G. (1972) *The Molecular Replacement Method*, Gordon & Breach, New York.
29. Navaza, J. (1993) *Acta Crystallogr. D 49*, 588−591.
30. Terwilliger, T. C., and Eisenberg, D. (1983) *Acta Crystallogr. A 39*, 813−817.
31. Read, R. J. (1986) *Acta Crystallogr. A 42*, 140−149.
32. Jones, T. A. (1985) *Methods Enzymol. 115*, 157−171.
33. Tronrud, D. E., Ten Eyck, L. F., and Matthews, B. W. (1987) *Acta Crystallogr. A 43*, 489−501.
34. Laskowski, R. A., MacArthur, M. W., Moss, D. S., and Thornton, J. M. (1993) *J. Appl. Crystallogr. 26*, 283−291.
35. Endow, S. A., and Komma, D. J. (1997) *J. Cell Biol. 137*, 1321−1336.
36. Fisher, A. J., Smith, C. A., Thoden, J. B., Smith, R., Sutoh, R., Holden, H. M., and Rayment, I. (1995) *Biochemistry 34*, 8960−8972.
37. Saunders, W. S., and Hoyt, M. A. (1992) *Cell 70*, 451−458.
38. Hoyt, M. A., He, L., Totis, L., and Saunders, W. S. (1993) *Genetics 135*, 35−44.
39. Woehlke, G., Ruby, A. K., Hart, C. L., Ly, B., Hom-Booher, N., and Vale, R. D. (1997) *Cell 90*, 207−216.
40. Sosa, H., Dias, D. P., Hoenger, A., Whittaker, M., Wilson-Kubalek, E., Sablin, E., Fletterick, R. J., Vale, R. D., and Milligan, R. A. (1997) *Cell 90*, 217−224.
41. Kraulis, P. J. (1991) *J. Appl. Crystallogr. 24*, 946−950.

BI972504O